


Influence of the Impaction Angle on the Triboelectric Charging of Aerosol Nanoparticles

Malte Bierwirth*, Manuel Gensch, and Alfred P. Weber

DOI: 10.1002/cite.202000196

 This is an open access article under the terms of the Creative Commons Attribution License, which permits use, distribution and reproduction in any medium, provided the original work is properly cited.



Supporting Information
available online

A low pressure impactor is used to measure triboelectric charging behavior of metallic nanoparticles. Ag nanoparticles, produced by spark discharge, were impacted onto Pt sputtered targets. The influence of the impaction angle and impaction velocity on the triboelectric charging was investigated. While for perpendicular impaction the charge transfer behavior of previous work was confirmed, the oblique impaction revealed new phenomena. Additional charge transfer was observable, which increases with obliqueness. The possibility of mass transfer between particle and target due to the high-energy collisions was also investigated. SEM characterization and Auger spectroscopy indicate mass transfer from the particle to the target surface.

Keywords: Charge transfer, Low pressure impactor, Mass transfer, Oblique impaction, Triboelectric charging

Received: September 01, 2020; *revised:* March 25, 2021; *accepted:* March 25, 2021

1 Introduction

Collisions of nanoparticles with walls are encountered during production and handling of powders and play an important role in dust separation and sampling of aerosol particles. During the particle-wall contact different phenomena such as impaction, sliding or rolling may be encountered. This can lead to deagglomeration [1–5], to adhesion and bouncing [6–9] as well as to charge transfer due to contact and triboelectric charging, respectively [5, 10–12]. Triboelectric charging is employed in technical applications such as printing toner particles [13] and, due to the strong material dependency on the charging characteristics, in powder sorting technologies [14]. While in the field of mineral processing and polymer sorting the process of triboelectric charging has been investigated thoroughly with typical diameters in the range from 100 μm to several mm [15, 16], for particle-wall collisions in the nanometer range there are still pieces missing in understanding the mechanisms at work.

For the charge transfer in particle-wall collisions, one of the main parameters is the contact potential between the two collision partners, which is given by the difference of both work functions [17]. To simplify the situation, the particle wall contact is often approximated as a capacitor with a characteristic time τ to obtain the charge equilibrium:

$$\tau = R_0 C \quad (1)$$

where R_0 is the resistance of the equivalent circuit and C is the capacity, which in turn is proportional to the contact area. For the system shown in Fig. 1a the charge Q transferred at a separation distance z is given by:

$$Q = C_0^*(z) \left(\frac{\Phi_T - \Phi_P}{e} \right) \quad (2)$$

where Φ_P is the particles work function, Φ_T is the work function of the target (impaction plate) and e is the elementary charge. The capacitance $C_0^*(z)$ of the particle-wall system depends on the permittivity of vacuum ϵ_0 , separation distance z and particle diameter d_p [10]:

$$C_0^*(z) = 2\pi\epsilon_0 d_p \left[1 + \frac{1}{2} \log \left(1 + \frac{d_p}{2z} \right) \right] \quad (3)$$

For conducting nanoparticles undergoing normal collisions with a conducting wall, the amount of transferred charge depends on the particle size and on the material combination, but within a certain velocity range does not depend on the impact velocity [4, 10]. Therefore, the charg-

Malte Bierwirth, Dr. Manuel Gensch,
Prof. Dr. rer. nat. Alfred P. Weber
malte.bierwirth@tu-clausthal.de
Clausthal University of Technology, Institute of Particle Technology,
Leibnizstraße 19, 38678 Clausthal-Zellerfeld, Germany.

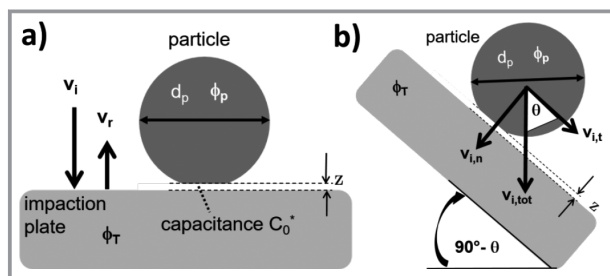


Figure 1. a) Normal impactation of a particle with diameter d_p and work function Φ_p on a target with work function Φ_T . The particle has the impact velocity v_i and the rebound velocity v_r . The system particle-plate defines a capacitance with a separation distance z (cf. Eq. (3)). b) Oblique impactation (under an angle θ) of a particle with total impact velocity $v_{i,tot}$, which is divided into a normal component $v_{i,n}$ and a tangential component $v_{i,t}$.

ing behavior is split into three regimes, insufficient rebound (regime A), equilibrium charge (regime B) and further charge increase (regime C). Rennecke and Weber [10] attributed the increase in transferred charge at low velocities to insufficient rebound due to the parabolic flow profile in the impactor. When all particles rebound, equilibrium charge q_e is reached and remains constant over a sizeable range of velocities. The equilibrium charge follows the capacitor model described by Eqs. (2) and (3). While charges between particle and target surface can also be exchanged without direct contact, this transfer ceases at a certain distance z_{tunnel} where the probability for electron tunneling vanishes. For even higher impact velocities, new phenomena come into play, which lead to a further charge transfer (regime C). The exact reasons for this effect are still unknown but may be related to additional surface defects due to plastic deformation [10].

Such additional surface states were found for polymer surfaces from quantum mechanical calculations and it was observed that these surface defects can have a substantial influence on the work function [18, 19]. Besides defects, the collisions can also result in the exchange of material between the colliding partners. In the size range of nanoparticles, such a material exchange has been demonstrated by molecular dynamics (MD) simulations [20]. However, the influence of oblique impactation on the charge transfer for nanoparticle-wall collisions was not studied so far. Therefore, the present study aims at the broadening of experimental database to facilitate the sound explanation of the triboelectric charging processes.

2 Experimental Setup

The experimental setup is shown in Fig. 2. Spherical Ag aerosol particles were produced

with a spark discharge generator (SDG). In the home-built SDG a capacitance of 50 nF was charged in parallel to two opposing Ag electrodes. As carrier gas nitrogen (purity of 5.0, Linde) was used at a flow rate of 1 L min⁻¹ to carry away the metal vapor, which was released in the discharge. The Ag agglomerates, which formed during the cooling behind the SDG by nucleation, condensation and agglomeration, were sintered to spherical particles in a tube furnace at 450 °C. Then, the aerosol particles achieved a Boltzmann charge distribution by passing a soft X-ray charger (Model 3088, TSI). Before classification with a radial differential mobility analyzer (RDMA, home-built), the excess aerosol was discarded through a filter. The concentration of the mobility-classified particles was monitored with a Faraday cup electrometer (FCE, home-built). The aerosol entered the low pressure impactor (LPI) through a critical orifice to keep the mass flow rate constant. In the subsequent nozzle, the aerosol was accelerated and directed towards the impaction plate. According to the desired impactation angle, different oblique impactation plates were employed. To guarantee a smooth impactation surface the plate was sputtered with a Pt film for all experiments. The charge of the non-impacting or bouncing particles was measured with a FCE (home-built). To obtain the characteristic inertial behavior of the particles (e.g., relaxation time), a deposition curve was determined for each system by covering the impaction plate with a vacuum grease to avoid bouncing. For the charge transfer measurements, no grease was applied and the change of particle charge, which was one elementary charge initially after classification with the DMA, was directly monitored with the FCE. In order to achieve a smooth scanning of the pressure range (typically from 5 mbar to 100 mbar), a vacuum tank was evacuated first, then the

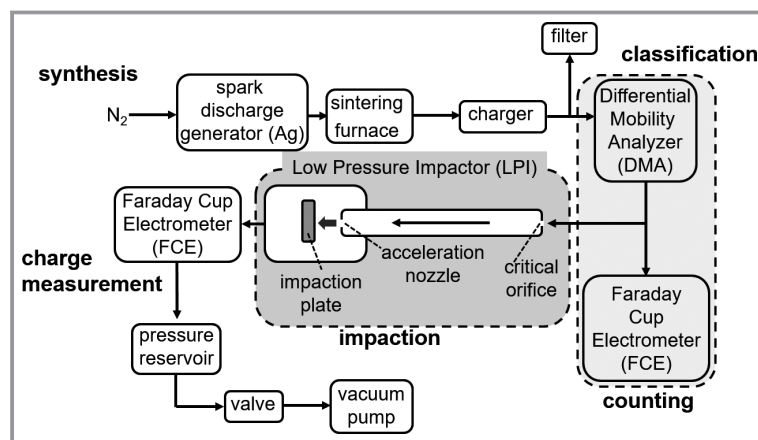


Figure 2. Schematic diagram of the experimental setup: Nanoparticles were produced by spark discharge generation followed by complete sintering to obtain spherical Ag particles; after charging in a soft X-ray charger monomobile particles were selected in a differential mobility analyzer (DMA), counted with a Faraday cup electrometer (FCE) and impacted on a target in a low pressure impactor (LPI). The impact velocity was varied via the pressure in the LPI and the impactation angle was chosen by tilting the target plate. Finally, the particle charge was measured with a second FCE. To avoid particle bouncing the impaction plate was coated with a vacuum grease for the separation measurements.

pump was stopped and the pressure in the system increased steadily as observed with a pressure gauge. In this way, a measurement started at low pressure, i.e., at high gas velocity, and raised according to the gas flow rate through the critical orifice.

3 Results and Discussion

The inclination of the impaction plate affects the flow field and the particle motion with respect to normal and tangential impact velocity. Therefore, before discussing the influence of the impact angle on the triboelectric charging, the behavior of the chosen geometry of the oblique impactor needs to be characterized. Then, the influence of the velocity components on the particle charging will be discussed for metallic nanoparticles impacting on a Pt target sputtered on a mica substrate.

3.1 Characterization of the Oblique Impaction

As already indicated in Fig. 1b in the case of oblique impaction only a fraction of the total velocity, i.e., the normal component, conducts the particles towards the wall [21]. In Fig. 3 the deposition curves for spherical 25 nm Ag particles, which are accelerated towards a greased mica target, are presented as a function of the chamber pressure. The absolute pressure determines the maximum gas velocity in the jet affecting also the particle impact.

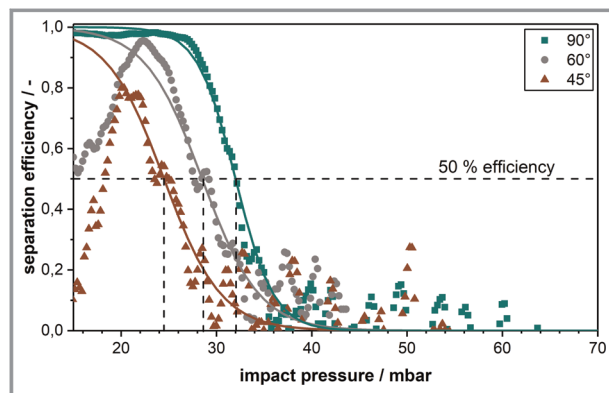


Figure 3. Deposition curves for 25 nm Ag nanoparticles on greased mica target as a function of the LPI pressure for three impaction angles: $\theta = 90^\circ$, 60° and 45° , including the model fits to measurements as lines in corresponding colors. Dashed vertical lines are the pressure values p_{50} where 50% of the particles are deposited.

With decreasing impact angle, the pressure to obtain 50% deposition of the particles is reduced, which means the total particle velocity has to increase. Reducing the pressure further leads for all angles to an improved deposition efficiency, while for 60° and 45° the fraction of deposited particles drops again for even lower pressures. This effect is

supposedly due to the phenomenon that at higher impact velocities the particles are again able to escape the greased target surface by a combination of rolling, gliding and bouncing. More details on the velocity calculation by Rennecke and Weber [22] and Gensch and Weber [21] can be found in the Supporting Information.

The lines in Fig. 3 (in corresponding colors) are fits of the separation efficiency S , which are calculated according to the following equation:

$$S = \frac{1}{1 + \exp\left(\frac{p - p_{50}}{\Delta p}\right)} \quad (4)$$

With p as the impaction pressure, p_{50} as the pressure 50% of particles are deposited, and Δp as the inverse sharpness of separation.

For the characterization of the oblique impaction behavior, the corresponding Stokes numbers Stk_{50}^* have been calculated for each inclination of the impaction plate. In contrast to the normal impaction, where L/D (with L as nozzle-to-plate distance, D as nozzle diameter) ratio is clearly defined, the corresponding effective L/D ratio for oblique impaction was adjusted by interpolation. With increasing L/D ratio the gas velocity is reduced by entrainment of surrounding gas also slowing down the particle velocity. Therefore, higher gas velocities are necessary to achieve the same degree of deposition. With an increasing obliquity, also the sharpness of cut decreases due to less severe deviation and a more asymmetric distribution of impact velocities and impact positions [21]. For a given Stokes number an increase of L/D ratio leads to reduced impaction angles because of the above-mentioned slowing of the jet velocity by gas entrainment. However, at high values of Stokes the particles are focused on the center line of the gas jet resulting in a narrower distribution of impact velocities and positions [21, 22].

In the following, the effective impact angle and the total impact velocity were used to separate the influence of normal and tangential particle motion during impact on the charge transfer. It will be argued that the normal velocity component is responsible for particle compression and contact time, while the tangential velocity components may lead to particle sliding and rolling due to friction forces.

3.2 Triboelectric Charging of Nanoparticles

To investigate the contact charging, Ag nanoparticles were impacted on a Pt sputtered mica target. For a given chamber pressure, the particle impact velocity was calculated using Eq. (S1). The results for the charging of particles bouncing from the Pt target after a normal impact ($\theta = 90^\circ$) are shown in Fig. 4 for three different size classes. Although there is some noise of the FCE signal, an initial regime of increasing bouncing efficiency (regime A), an equilibrium regime (regime B) and an additional increase of particle

charge at very high impact velocities (regime C) are discernable in good correspondence with former measurements (see [10]). The onset of the last increase of the particle charge (beginning of regime C) is shifted to the right with decreasing particle size. In fact, for the smallest measured particles of 15 nm this last increase is not observed within the velocity range accessed in the present setup. However, the equilibrium charges agree well with the former results for the system Ag nanoparticles on Pt target [10]. This means also that the amount of transferred charges is in agreement with the capacitor model presented in Eqs. (2) and (3). Using the capacitor model and the data shown in Fig. 4 the difference $\Delta\phi$ of the work functions of Ag and Pt is calculated to be

$$\Delta\phi_{\text{exp}} = \phi_{\text{Pt}} - \phi_{\text{Ag}} \approx 0.3 \text{ eV} \quad (5)$$

(assuming $z_{\text{tunnel}} \approx 1 \text{ nm}$), which is in reasonable agreement with values from the literature for ultraclean surfaces [10]:

$$\begin{aligned} \Delta\phi_{\text{theo}} &= \phi_{\text{Pt}} - \phi_{\text{Ag}} \approx 5.3 \text{ eV} - 4.7 \text{ eV} \\ &= 0.6 \text{ eV} \end{aligned} \quad (6)$$

This difference should be evaluated considering the purity of the interacting surfaces. During the synthesis of the particles, some oxidation cannot be prevented. Additionally, a possible accumulation of water vapor on the target surface should be assumed. Despite this, the difference is reasonably close to the theoretical value.

The reason for the last increase of the particle charge (regime C, in Fig. 4) is not known so far. It could be related to the onset of plastic deformation, which may lead to defects. Such defects have been predicted as a consequence of plastic deformation [22] but were also observed under the influence of friction [18]. Surface defects may have a substantial influence on the work function [23, 24]. In order to uncover the effect of a tangential velocity component, which could induce friction, 45 nm Ag nanoparticles were impacted onto a Pt target under a nominal angle of 45° and 60° , respectively. The results of particle charging for normal and oblique impaction are compared in Fig. 5. To elucidate the effect of the impaction angle, the total transferred charge is plotted

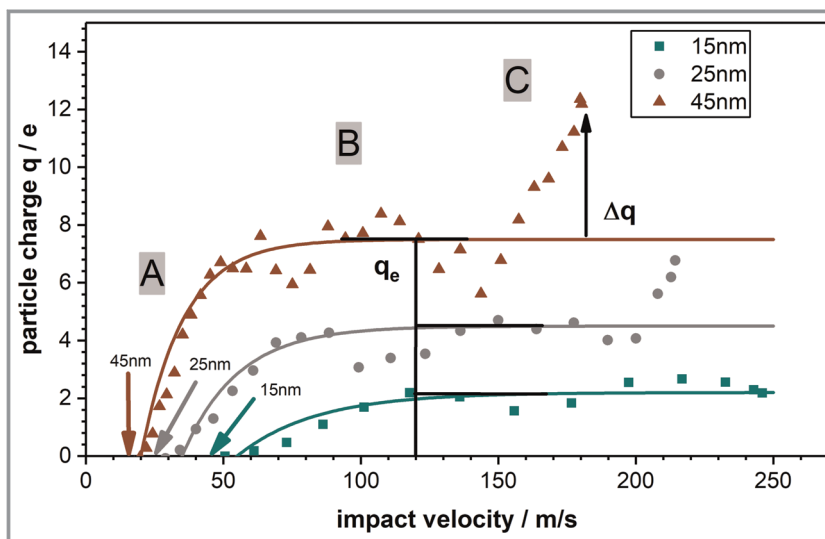


Figure 4. Charging of Ag particles impacting normally ($\theta = 90^\circ$) on a Pt target as a function of the impact velocity: The three regimes indicate: insufficient rebound (regime A), equilibrium charge (regime B), and further charge increase (regime C). Particle sizes are 15, 25 and 45 nm and arrows indicate respective critical rebound velocity, i.e., the minimum impaction velocity for rebound (obtained at the jet center line).

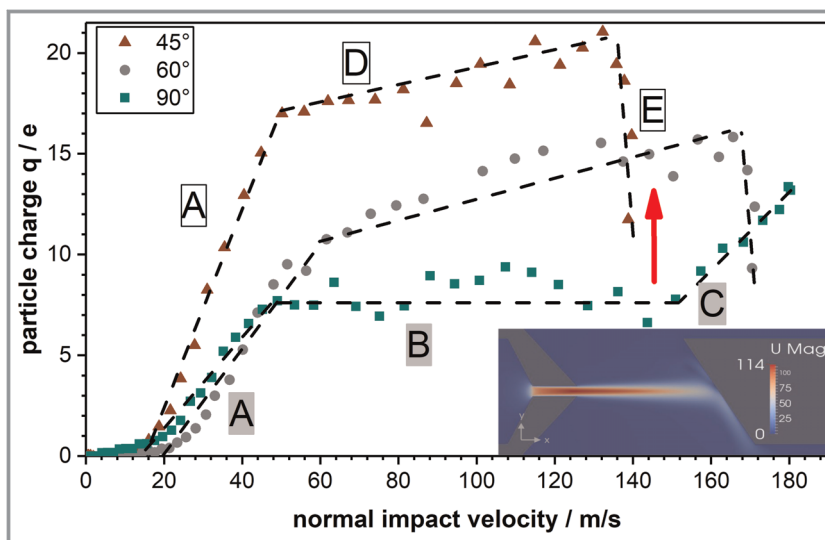


Figure 5. Charging of 45 nm Ag particles impacting on a Pt target as a function of the normal impact velocity under normal ($\theta = 90^\circ$) and oblique impaction ($\theta_{\text{nom}} = 45^\circ$ and 60°). A: zone of approaching complete rebound; B: equilibrium charge; C: additional charge transfer; D: continuous charge increase; E: sudden drop of particle charge. The red arrow indicates an increase of the achieved particle charge by the additional tangential velocity component for oblique impaction. The inset is showing the gas flow profile at oblique impaction [25].

against the normal component of the impact velocity. Considering only the normal component bouncing starts for all angles at roughly the same impact velocity. However, even in regime A for impaction at 45° the transferred charge is significantly higher than the charge transfer for normal impaction and oblique impaction at 60° . According to the remarks above, this could be due to an increase of the particle work function as a result of surface defects initiated by

friction. The higher tangential forces at 45° lead to an increased amount of friction. For both impaction types, the particle charge increased from the equilibrium level (regime B) to higher values when increasing the impaction velocity further (regime C). For oblique impaction, the continuous charge increase (regime D) can probably be attributed to a superposition of the equilibrium charge (regime B) and additional charge transfer (regime C). It is assumed that the tangential forces during impaction already start to generate friction, which causes defects in the particle surface. Therefore, the charge increases continuously with the impact velocity.

In order to extract the influence of the tangential velocity component more evidently, the following subtraction model was employed: It was assumed that normal and tangential charging mechanisms are additive and that they can be separated by simply subtracting the normally transferred equilibrium charge from the totally transferred charge. This procedure does not take into account the lower particle charges for normal impaction velocities below 50 m s^{-1} (zone A) and the higher particle charges for normal impaction above 170 m s^{-1} (zone C). However, for the investigated oblique impaction angles, these lower and upper regimes cannot be accessed since no information about the particle charge for normal impaction velocities below 50 m s^{-1} are available (no rebound) and normal impaction velocity components did not exceed 170 m s^{-1} . The total particle charge reduced by the equilibrium charge will be called *tangential* charge q_t , which is shown in Fig. 6 as a function of the tangential velocity component for oblique impaction under 45° and 60° . The tangential velocity components were determined using Eq. (S2).

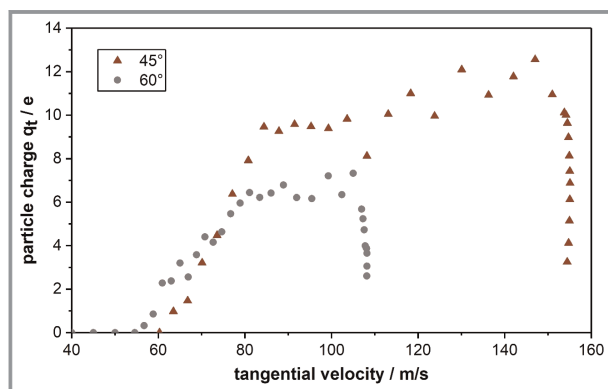


Figure 6. Acquisition of *tangential* charge q_t of 45 nm Ag particles impacting on a Pt target as a function of the tangential velocity under $\theta = 60^\circ$ (gray dots) and $\theta = 45^\circ$ (red triangles). q_t was obtained by subtracting the equilibrium charge acquired from normal impaction from the total charge (cf. Fig. 5).

For both oblique angles there is the same onset tangential velocity for the particle charging and a significant charge loss at high velocities. For $\theta = 45^\circ$ the attained charge levels are higher and the onset of charge drop occurs at higher velocities than in the case of 60° . The fact that particles can

lose charge is rather surprising. There are a few possible explanations. Firstly, a local gas breakdown may occur leading to neutralization of the particles. However, in this regime of surface separation the well-known Paschen curve is not applicable anymore. Since the mean free path in the low-pressure environment is in the range of microns and the separation distance of particle-wall around 1 nm, there is simply no gas available to introduce a gas breakdown. Secondly, as indicated by MD simulations [23], material can be exchanged between the contacting partners. According to the condenser model this would result in carrying away of the opposite charge with the particles or deposition of charges due to particle fragmentation. Therefore, reduced charge separation would take place. Such a material transfer was indeed observed for larger particles subjected to multiple perpendicular contacts [26]. To prove that this mechanism is in fact at work at high tangential velocities, particles were impacted for a long time at a constant high velocity (constant low pressure), to magnify this effect for further analysis.

The so treated Pt target was then introduced into a SEM and the micrographs seen in Fig. 7 were taken. The micrograph a) shows an area that seems slightly darker under the microscope. This spot is barely visible to the naked eye. The seen rough scratches were carved onto the target to be able to find the spot while in the SEM. The micrograph b) shows the darker spot at a higher magnification of 5000. In addition, high-resolution SEM (HR-SEM) characterization and Auger electron spectroscopy (AES) were performed. The micrograph c) was taken outside of this dark spot, while the micrograph d) was taken inside. In the micrographs c) and d) a clear difference in the target surface is visible with a high magnification of 182 000. Particles and particle fragments can be seen in micrograph d) and with AES Ag was

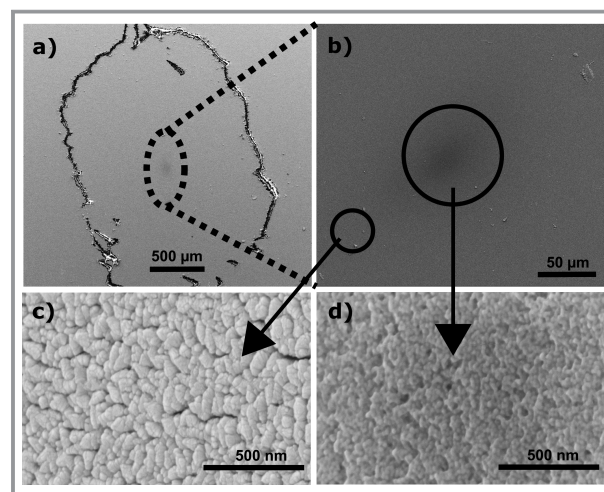


Figure 7. SEM micrographs of 120 nm Pt sputtered mica target after bombardments for 25 min at constant velocity. a) Overview with a visible darker spot (dotted ellipse), b) darker spot at a higher magnification, c) taken at a point outside the dark spot, d) inside the dark spot.

clearly identified as the surface element, whereas Pt was not measured on the surface in the same area. This indicates a complete layer of Ag at least 2 nm thick, as AES is only able to penetrate the surface up to a few nm.

Moving the observation area more to the outside of the center point, Ag was detected even in areas without visible surface change. This would indicate a transition area where only fragments of particles are left behind after impact, which are not easily resolved even in HR-SEM. Additional energy-dispersive X-ray spectroscopy (EDX) measurement were conducted, which detected Ag and Pt simultaneously, even in the center point. Since EDX penetrates the target up to 2 microns in depth, this is to be expected. With several spot measurements, moving through the area of interest, a surface loading was determined. Under the assumption that in the center the coverage is 1, which is supported by the AES, radial Ag profiles were measured whereas in the outside regions the coverage dropped to 0. These results are presented in Fig. 8.

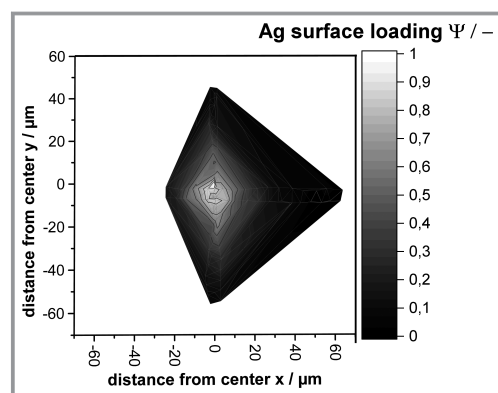


Figure 8. Surface loading of the 120 nm Pt sputtered mica target with Ag. Combined and normalized results of EDX measurements and AES. (x,y) coordinates correspond to the position of the spot measurement, the grayscale indicates the amount of loading.

To summarize the behavior at these very high velocities, the following process is hypothesized: Ag particles impact on the clean sputtered Pt surface at high velocities and rebound, leaving fragments behind, which explain the loss of charge. With increasing time more and more fragments lead to an Ag-loaded surface, which then does not promote rebound from further incoming particles. The additional particles impact, deform and lead to the surface structure observed in Fig. 7d. For the charge transfer measurements, this high velocity regime is only present for a short time, which is not long enough to change the surface and influence rebound at lower velocities. There still is the possibility of additional mass transfer from the target surface onto the particle material, which is very hard to quantify and considering the different yield stress of the particle and target material this seems unlikely. It can play a more significant role in other material combinations. Further experimental investigations and MD simulations are necessary to

improve the understanding of material transfer during low pressure impactation of nanoparticles.

4 Summary

The influence of the impactation angle on the charge transfer was investigated for nanoparticles rebounding from a Pt target. While for perpendicular impact previous results were confirmed, the oblique impact revealed new phenomena. For normal impactation at moderate velocities, the classical condenser model had proven to be applicable for metal-metal contacts leading to an equilibrium charge as a result of the equilibration of the contact potential. However, for oblique metal-metal contacts the transferred charge increases first with velocity and then drops suddenly towards zero, which could indicate a material transfer from the Ag nanoparticles to the Pt plate. In fact, such a material transfer was confirmed by AES measurements and SEM micrographs. This means that at the contact zone, where charge transfer takes place, material is left behind with the target surface largely annihilating the particle charge. The outlined experimental technique allows for an improved understanding of triboelectric charging effects of nanoparticles. Nevertheless, the phenomena on the atomistic and molecular level can only be elucidated with further molecular dynamics simulations, which couple the charge transfer with the surface modifications during impactation and rebound.

Supporting Information

Supporting Information for this article can be found under DOI: <https://doi.org/10.1002/cite.202000196>.

The authors would like to thank the Institute of Energy Research and Physical Technologies for their help with the SEM imaging and Auger electron spectroscopy, especially Wanja Dziony and Dr. Lilienkamp. Funded by the Deutsche Forschungsgemeinschaft (DFG, German Research Foundation) – Project ID 394563137 – SFB 1368. Open access funding enabled and organized by Projekt DEAL.

Symbols used

| | | |
|---------|------|-------------------------------------|
| C | [F] | capacitance |
| C_0^* | [F] | capacitance of particle-wall system |
| D | [mm] | nozzle diameter |
| d_p | [nm] | particle diameter |
| E | [-] | empirical constant |
| e | [C] | elementary charge |
| F | [-] | empirical constant |
| G | [-] | empirical constant |

| | | |
|------------------------|-----------------------|-------------------------------------|
| H | [mm] | nozzle length |
| L | [mm] | distance nozzle to impaction plate |
| \dot{m}_{gas} | [kg s ⁻¹] | gas mass flow |
| p | [mbar] | pressure |
| p_{50} | [mbar] | pressure at 50% deposition |
| Q | [e] | transferred charge |
| q | [e] | particle charge |
| q_e | [e] | particle charge equilibrium |
| q_t | [e] | tangential particle charge |
| R_0 | [Ω] | resistance |
| S | [-] | separation efficiency |
| Stk | [-] | Stokes number |
| Stk_{50} | [-] | Stokes number at 50% deposition |
| v_i | [m s ⁻¹] | particle impact velocity |
| $v_{i,n}$ | [m s ⁻¹] | normal particle impact velocity |
| $v_{i,t}$ | [m s ⁻¹] | tangential particle impact velocity |
| $v_{i,tot}$ | [m s ⁻¹] | total particle impact velocity |
| \bar{v}_i | [-] | dimensionless impact velocity |
| $v_{\text{max,gas}}$ | [m s ⁻¹] | maximum gas velocity |
| v_r | [m s ⁻¹] | particle rebound velocity |
| z | [nm] | separation distance |

Greek letters

| | | |
|-----------------------|----------------------|---------------------|
| θ | [°] | angle |
| Ψ | [-] | surface loading |
| ϵ_0 | [F m ⁻¹] | vacuum permittivity |
| τ | [s] | characteristic time |
| Φ | [eV] | work function |
| θ_{eff} | [°] | effective angle |
| θ_{nom} | [°] | nominal angle |
| χ_{lag} | [-] | lag factor |

Sub- and Superscripts

| | |
|------|--------------|
| * | modified |
| e | equilibrium |
| eff | effective |
| exp | experimental |
| p | particle |
| T | target |
| theo | theoretical |

Abbreviations

| | |
|--------|--|
| AES | Auger Electron Spectroscopy |
| EDX | Energy-dispersive X-Ray spectroscopy |
| FCE | Faraday Cup Electrometer |
| LPI | Low Pressure Impactor |
| RDMA | Radial Differential Mobility Analyzer |
| SDG | Spark Discharge Generator |
| SEM | Scanning Electron Microscope |
| HR-SEM | High Resolution Scanning Electron Microscope |

References

- [1] M. Seipenbusch, S. Froeschke, A. P. Weber, G. Kasper, *Proc. Inst. Mech. Eng., Part E* **2002**, 216 (4), 219–225. DOI: <https://doi.org/10.1243/095440802321194495>
- [2] M. Seipenbusch, S. Rothenbacher, M. Kirchhoff, H. J. Schmid, G. Kasper, A. P. Weber, *J. Nanopart. Res.* **2010**, 12 (6), 2037–2044. DOI: <https://doi.org/10.1007/s11051-009-9760-5>
- [3] M. Seipenbusch, P. Toneva, W. Peukert, A. P. Weber, *Part. Part. Syst. Charact.* **2007**, 24 (3), 193–200. DOI: <https://doi.org/10.1002/ppsc.200601089>
- [4] R. Wernet, D. Nazarenus, M. Seipenbusch, *J. Aerosol Sci.* **2017**, 110, 1–10. DOI: <https://doi.org/10.1016/j.jaerosci.2017.05.002>
- [5] M. Gensch, A. P. Weber, *Chem. Ing. Tech.* **2014**, 86 (3), 270–279. DOI: <https://doi.org/10.1002/cite.201300134>
- [6] M. Gensch, A. P. Weber, *Adv. Powder Technol.* **2017**, 28 (8), 1930–1942. DOI: <https://doi.org/10.1016/j.apt.2017.05.003>
- [7] S. Rennecke, A. P. Weber, *J. Aerosol Sci.* **2013**, 58, 135–147. DOI: <https://doi.org/10.1016/j.jaerosci.2012.12.007>
- [8] H.-C. Wang, G. Kasper, *J. Aerosol Sci.* **1991**, 22 (1), 31–41. DOI: [https://doi.org/10.1016/0021-8502\(91\)90091-U](https://doi.org/10.1016/0021-8502(91)90091-U)
- [9] M. Heim, B. J. Mullins, M. Wild, J. Meyer, G. Kasper, *Aerosol Sci. Technol.* **2005**, 39 (8), 782–789. DOI: <https://doi.org/10.1080/02786820500227373>
- [10] S. Rennecke, A. P. Weber, *Aerosol Sci. Technol.* **2014**, 48 (10), 1059–1069. DOI: <https://doi.org/10.1080/02786826.2014.955566>
- [11] P. M. Ireland, *Powder Technol.* **2010**, 198 (2), 199–210. DOI: <https://doi.org/10.1016/j.powtec.2009.11.008>
- [12] P. M. Ireland, *Powder Technol.* **2010**, 198 (2), 189–198. DOI: <https://doi.org/10.1016/j.powtec.2009.11.017>
- [13] L. B. Schein, *J. Electrostat.* **1999**, 46 (1), 29–36. DOI: [https://doi.org/10.1016/S0304-3886\(98\)00056-4](https://doi.org/10.1016/S0304-3886(98)00056-4)
- [14] M. J. Pearse, M. I. Pope, *Powder Technol.* **1977**, 17 (1), 83–89. DOI: [https://doi.org/10.1016/0032-5910\(77\)85045-6](https://doi.org/10.1016/0032-5910(77)85045-6)
- [15] S. Trigwell, K. B. Tennal, K. Malay, M. K. Mazumder, D. A. Lindquist, *Part. Sci. Technol.* **2003**, 21 (4), 353–364. DOI: <https://doi.org/10.1080/716100576>
- [16] J. R. Mountain, M. K. Mazumder, R. A. Sims, D. L. Wankum, T. Chasser, P. H. Pettit, *IEEE Trans. Ind. Appl.* **2001**, 37 (3), 778–784. DOI: <https://doi.org/10.1109/28.924759>
- [17] T. Matsuyama, H. Yamamoto, *Chem. Eng. Sci.* **2006**, 61 (7), 2230–2238. DOI: <https://doi.org/10.1016/j.ces.2005.05.003>
- [18] K. Yanagida, O. Okada, K. Oka, *Jpn. J. Appl. Phys.* **1993**, 32, 5603–5610. DOI: <https://doi.org/10.1143/JJAP.32.5603>
- [19] Y. Shirakawa, N. Li, M. Yoshida, R. Takashima, A. Shimosaka, J. Hidaka, *Adv. Powder Technol.* **2008**, 21 (4), 500–505. DOI: <https://doi.org/10.1016/j.apt.2010.05.007>
- [20] S. Solhjoo, A. I. Vakis, *Comput. Mater. Sci.* **2015**, 99, 209–220. DOI: <https://doi.org/10.1016/j.commatsci.2014.12.010>
- [21] M. Gensch, A. P. Weber, *Adv. Powder Technol.* **2018**, 29 (12), 3462–3470. DOI: <https://doi.org/10.1016/j.apt.2018.09.029>
- [22] S. Rennecke, A. P. Weber, *J. Aerosol Sci.* **2013**, 55, 89–103. DOI: <https://doi.org/10.1016/j.jaerosci.2012.07.014>
- [23] S. Matsusaka, H. Maruyama, T. Matsuyama, M. Ghadiri, *Chem. Eng. Sci.* **2010**, 65 (22), 5781–5807. DOI: <https://doi.org/10.1016/j.ces.2010.07.005>
- [24] W. Li, D. Y. Li, *Mater. Sci. Technol.* **2002**, 18 (9), 1057–1060. DOI: <https://doi.org/10.1179/026708302225005918>
- [25] M. Gensch, *Mechanische Stabilität von Nanopartikel-Agglomeraten bei mechanischen Belastungen*, Ph.D. Thesis, TU Clausthal **2018**.
- [26] B. A. Kwetkus, K. Sattler, *J. Phys. D: Appl. Phys.* **1992**, 25 (10), 1400–1408. DOI: <https://doi.org/10.1088/0022-3727/25/10/004>